Xenocryst assimilation and formation of peritectic crystals during magma contamination: An experimental study

Saskia Erdmann, Bruno Scaillet, D.A. Kellett

▶ **To cite this version:**

HAL Id: insu-00534451

https://hal-insu.archives-ouvertes.fr/insu-00534451

Submitted on 16 Dec 2010

Xenocryst assimilation and formation of peritectic crystals during magma contamination: An experimental study

S. Erdmann[a, b,] , B. Scaillet[a] and D.A. Kellett[c]

[a] Centre National de la Recherche Scientifique, Institut des Sciences de la Terre d'Orléans, France

[b] Université de Genève, Département de Minéralogie, Switzerland

[c] Dalhousie University, Department of Earth Sciences, Canada

Abstract

Contamination of magmas by country rocks may contribute xenoliths and xenocrysts to the magma, but also melt and peritectic crystals that form through incongruent melting or dissolution of the original contaminants. Identifying contaminant-derived peritectic crystals and former melt components in igneous rocks is particularly challenging, but also particularly important, because their assimilation significantly affects melt composition and magma temperature. To facilitate the identification of peritectic crystals in igneous rocks, the aim of this study was to experimentally control partial assimilation of xenocrysts and examine the formation, textures, and composition of resulting peritectic crystals. Our experiments mimic contaminant melting and contamination of a partially crystallized basaltic andesite by melanorite- and monzodiorite-derived xenocrysts and micro-xenoliths. Micro-xenoliths and xenocrysts partially survive assimilation, and yet peritectic crystals form ~ 1/3 of all solid contaminants. Anhydrous xenocrysts either develop laterally continuous, subhedral to euhedral, and inclusion-poor overgrowths, or progressively decompose. Hydrous and partially altered xenocrysts decompose to peritectic crystals. The peritectic crystals form clusters of subhedral to euhedral, randomly-oriented olivine, clinopyroxene, olivine–plagioclase, and olivine–plagioclase–clinopyroxene that texturally resemble primary magmatic crystals. We propose that natural peritectic crystals with short residence times form clusters of one or more minerals with textures as those of our experiments, and that peritectic crystals with longer residence times likely anneal to subhedral or euhedral single crystals or coarse-grained mineral clusters. They hold crucial evidence for largely assimilated country-rock components and estimates of open-system magma evolution, but the longer their magma residence time the more easily they are overlooked.

Keywords: assimilation; contamination; peritectic crystal; experiment; texture

1. Introduction

Crystals in igneous rocks may be primary, cognate magmatic, inherited from the source, derived from country rocks or magma mixing, or secondary magmatic (e.g., [Stewart, 1975], [Couch et al., 2001], [Stephens, 2001], [Amma-Miyasaka and Nakagawa, 2002], [Beard et al., 2005], [Clarke, 2007], [Stevens et al., 2007] and [Streck, 2008]). Country-rock-derived crystals, which are the focus of our contribution, may include xenocrysts and peritectic crystals that formed through incongruent melting or dissolution of xenocrysts and xenoliths ([Lackey et al., 2006], [Clarke, 2007] and [Erdmann et al., 2009]). Detecting their presence in igneous rocks may be challenging, but contributes important constraints on closed- versus open-system magma evolution that in turn guide geochemical and thermodynamic modelling.

Refractory contaminants, although they survive assimilation as xenoliths or xenocrysts, may nevertheless be compositionally or texturally modified by assimilation reactions. Fertile contaminants may largely react to peritectic crystals, melt, or fluids, leaving little or no direct evidence (e.g., [Clarke, 2007], [Iacono-Marziano et al., 2007] and [Erdmann et al., 2009]). Xenoliths and exotic xenocrysts are easily, and thus commonly identified, but peritectic crystals and xenocrysts with compositions and textures resembling those of primary magmatic crystals are more difficult to detect, and thus rarely reported. The purpose of this study is to improve identification of xenocrysts and peritectic crystals formed through contamination in igneous rocks by studying products of experimental magma contamination. We use the terms "xenocrysts" to refer to solids inherited from original contaminants and "peritectic crystals" to refer to solid products of contaminant melting that form in a reaction of the type xenocrysts ± host melt = peritectic crystal(s) + melt.

We present experiments that simulate contaminant melting and contaminant–magma interaction and run products that reveal textural and compositional characteristics of partially assimilated xenocrysts and peritectic crystals. As starting materials for our experiments, we employed a basaltic andesite of the Holocene to ~ 930 ka Tatara–San Pedro (TSP) complex of the Southern Volcanic Zone of central Chile, and pre-Holocene melanorite and monzodiorite basement rocks ([Gonzàlez and Vergara, 1962], [Singer et al., 1997], [Nelson et al., 1999] and [Dungan et al., 2001]; and references therein). We chose these starting materials in order to focus our study on contamination of a common arc magma and because contaminants in lavas of the TSP volcanic complex appeared to include xenocrysts and peritectic crystals that served as a reference. Later, we describe our experimental rationale, experimental materials and methods, and run products. We then discuss the implications of our chosen experimental conditions, xenocryst assimilation, and the formation, textures, and composition of peritectic crystals resulting from magma contamination.

2. Experimental rationale, materials, and methods

2.1. Experimental rationale

To examine partial assimilation of xenocrysts and to identify textural and chemical characteristics of peritectic crystals resulting from contamination, we have performed three types of experiments: crystallization, contamination, and melting experiments (Fig. 1). We first crystallized a basaltic–andesitic glass (Fig. 1b; crystallization experiment C1). We then added an amphibole–phlogopite melanorite contaminant to the partially crystallized basaltic andesite (Fig. 1c; contamination experiment C2) and subsequently added a monzodiorite contaminant (Fig. 1d; contamination experiment C3). Contamination was carried out in two separate experiments to clearly distinguish between the effects of the two different contaminants. Starting materials were selected to mimic contamination of a common arc magma by two fertile contaminants. In particular, characterizing the assimilation of amphibole was of interest, as it is likely an important reactive contaminant in arc crust (Davidson et al., 2007). Two melting experiments employing the melanorite contaminant (Fig. 1e; melting experiments M1 and M2) were performed to constrain the role of host magmas on xenocryst assimilation and formation of peritectic crystals.

2.2. Starting materials

Raw starting materials for our experiments were a basaltic andesite (BA), an amphibole–phlogopite melanorite (MN), and a monzodiorite (MD) ([Table 1] and [Table 2]). The BA and

MN are calc-alkalic and have medium-K_2O compositions. The MD is calc-alkalic and relatively rich in K_2O. The BA has high V and Nb concentrations, but all other trace-element concentrations are intermediate between those of the MN and the MD contaminants.

The basaltic–andesitic starting rock belongs to the Middle Estero Molino sequence of the TSP complex, as defined by Dungan et al. (2001). It has ~15 vol.% macrocrystic olivine, plagioclase, and clinopyroxene (phenocrysts > 0.5 mm) set in a matrix of plagioclase, clinopyroxene, olivine, oxides (dominantly magnetite), and minor orthopyroxene. It does not contain glass. Potential contaminants in our BA starting rock and other TSP lavas include: (i) crystal clusters dominated by olivine and plagioclase with healed micro-fractures, subgrains, and deformation twins (Fig. 2a); (ii) olivine with grain-boundary melt film pseudomorphs (Fig. 2b); (iii) single crystals and clusters of subhedral olivine (Fig. 2c,d); (iv) complexly zoned clinopyroxene (Fig. 2e); and (v) skeletal to anhedral cores of plagioclase (Fig. 2f) (Dungan and Davidson, 2004; this study). Compositions of xenocrysts and potential peritectic crystals in TSP lavas show a wide range. In the studied BA, olivine has ~ Fo_{78-75} (core) to ~ Fo_{73-71} (rim) composition, plagioclase is ~ An_{82-72} (including spongy-cellular cores), and clinopyroxene is ~ $En_{47-40}Fs_{18-10}Wo_{45-40}$ with X_{Mg} values of ~ 83–70. Plagioclase xenocrysts from a TSP dacite flow have ~ An_{86-74}, including spongy-cellular cores (Singer et al., 1995). Olivine xenocrysts from a basaltic TSP lava flow have ~ Fo_{85-79} (core) to ~ Fo_{78-72} (rim) composition ([Dungan and Davidson, 2004] and [Costa and Dungan, 2005]. The starting glass produced from the BA includes components from ~5 vol.% micro-xenoliths and xenocrysts and therefore mimics one further increment of contamination rather than a first event.

The MN contaminant we employed is a Group IIHN xenolith from a TSP dacite flow, as defined by Costa et al. (2002) ([Table 1] and [Table 2]; Fig. 2g). It is dominated by euhedral to subhedral, unzoned plagioclase. A dominant mode has An_{85-80} composition, but few crystals have An_{80-50} composition (Table 3; Costa et al., 2002). Orthopyroxene, amphibole, and phlogopite form large, anhedral crystals with inclusions of olivine, plagioclase, and oxides (i.e. chromite, ulvöspinel, magnetite, and ilmenite). Orthopyroxene is enstatite (~ En_{78},Fs_{20},Ws_2; X_{Mg} ~ 80). Amphibole is Ti-rich and phlogopite is Na-rich. Olivine is subhedral to euhedral, forsterite-rich (~ Fo_{78}), and contains abundant oxide inclusions. All mafic minerals are largely unzoned in Mg and Fe. Olivine is partially altered to iddingsite along grain boundaries and microcracks. All other minerals exhibit little evidence for alteration.

The MD contaminant we employed ([Table 1] and [Table 2]; Fig. 2h) was sampled from the Cerro Risco Bayo pluton, which is one of several older plutons intruded by the volcanic TSP complex (Nelson et al., 1999). Plagioclase is subhedral to euhedral and normally zoned with labradorite to oligoclase composition (~ An_{55-30}; Table 3). Clinopyroxene forms subhedral to euhedral phenocrysts with aluminian augite composition (~ En_{38},Fs_{33},Ws_{29}). Biotite is subhedral and Mg-rich (X_{Mg} ~ 80). K-feldspar, oxides (predominantly magnetite), and quartz are small, subhedral, and unzoned. Plagioclase and K-feldspar are partly seriticized, clinopyroxene is partially replaced by fine-grained chlorite, and minor secondary epidote is present. The sample therefore best represents upper crustal contaminants affected by low-temperature alteration.

To prepare the experimental starting materials, the BA was ground to a powder and fused twice for ~4 h at 1400 °C and atmospheric conditions. Between and after fusing, the glass was ground to < 20 μm in an agate mortar. The coarse-grained MN and MD rocks were crushed to

a powder of ≤ 170 μm that predominantly consists of crystal fragments and few micro-xenoliths. Subsequently, powders were homogenized in an agate mortar to ensure that xenocrysts of each mineral type were added to the charges.

2.3. Experimental and analytical methods

Our two melting experiments employed MN powder and 1.1 wt.% (melting experiment M1) and 2.1 wt.% (melting experiment M2) deionized, ultrafiltered H_2O (Table 2). For our crystallization experiment a charge was loaded with 1.5 wt.% deionized, ultrafiltered H_2O and the basaltic–andesitic glass (crystallization experiment C1). After the experiment was terminated, small fragments of the run product were examined and analyzed by electron microprobe. The rest of the charge was ground to ~ 20–50 μm in an agate mortar, and mixed with 25 wt.% of the starting MN powder. A second charge (MN contamination experiment C2) was loaded with this mixture. No H_2O was added to the run, but ~ 27 and 5 vol.% of amphibole and phlogopite in the contaminant liberated 0.5–1 wt.% H_2O. Following the experiment, run products were divided for analysis and our second contamination experiment (MD contamination experiment C3), which employed a mixture of ground C2 run product and 5 wt.% MD powder.

The experiments were carried out at the ISTO-CNRS Orléans in an internally heated pressure vessel. Pressure was obtained by sequentially loading a mixture of Ar and H_2 gas at room temperature (e.g., Scaillet et al., 1995). The experimental temperature was reached in ~ 1.5 h; cooling of the charges was achieved by drop quench. Experimental fH was recorded using Ni–Pd–NiO solid sensors; experimental fO_2 was calculated from these sensors using the calibration of Pownceby and O'Neill (1994). All experiments were run for 24 h in $Au_{80}Pd_{20}$ capsules at 1085 °C, ~ 200 MPa, and fO_2 of ~ NNO + 0.9. We chose these conditions to simulate temperature and pressure conditions that have been estimated for contamination and partial crystallization of some TSP magmas ([Costa et al., 2004] and [Costa and Dungan, 2005]), at redox conditions typical for arc magmas (e.g., Behrens and Gaillard, 2006). A run duration of 24 h was used to concomitantly minimize Fe loss, achieve equilibrium in our crystallization experiment, and preserve disequilibrium textures in our contamination experiments (at least for larger xenocrysts and peritectic crystals). We also chose $Au_{80}Pd_{20}$ containers to minimize Fe loss (cf. [Kawamoto and Hirose, 1994], [Hall et al., 2004] and [Di Carlo et al., 2006]), but decreasing FeO content of olivine and glass from C1 to C3 shows that Fe loss took place. Mass-balance calculations for C1, M1, and M2 and compositions of C2 versus C3 run products suggest that Fe loss was probably between ~ 26 and 45% in the experiments (Table 5). We return to this point in the discussion (Section 4.1), but note here that the textural observations on xenocrysts and peritectic crystals are not compromised by this limitation. We also considered that the intended fO_2 of experiment C1 may not have been fully achieved owing to the high redox state of the starting glass. However, Fe^{3+}/Fe^{2+} re-equilibration is fast for the type of experiments performed and the absence of Fe oxides moreover suggests reduced fO_2 conditions (e.g., Gaillard et al., 2002).

Whole rock major- and trace-elements of starting material rock powders were analyzed by X-ray fluorescence at the Geochemical Centre of the Department of Geology at Saint Mary's University. Starting materials and experimental run products were characterized by back-scattered electron microscopy at Dalhousie University and at the ISTO-CNRS Orléans. Mineral compositions were determined using a JEOL 8200 electron microprobe at Dalhousie University; glass compositions were determined using a JEOL 733 electron microprobe at the Ontario Museum of Nature. For olivine and clinopyroxene, we refer to a core-rim decrease in

Fe and an increase in Mg as reverse zoning. For plagioclase, we describe a core-rim decrease in Ca and Al and an increase in Na and Si as normal zoning. Mineral-melt partition coefficients presented are $(Fe/Mg)_{Ol}/(Fe/Mg)_{Gl}$, $(Fe/Mg)_{Cpx}/(Fe/Mg)_{Gl}$ (total Fe as FeO), and $(Ca/Na)_{Pl}/(Ca/Na)_{Gl}$. Details of analyses are given in relevant figures and tables.

Modal assemblages of starting materials were estimated from thin sections, and modal assemblages of run products were estimated using back-scattered electron images and the Scion Image software. Errors are on the order of 5% at >20 vol.%, < 10% at 20–5 vol.%, and > 10% at <5 vol.%. In our description, we classify crystals in C1 and small, single, subhedral to euhedral crystals in C2 and C3 as primary magmatic (Ol1, Pl1, and Cpx1). We refer to crystals of the starting contaminants as xenocrysts (Ol2, Pl2, Opx2, Ox2 = MN xenocrysts; Pl4 = MD xenocryst). Crystals that are absent from the starting materials and C1 and that typically form clusters are interpreted as peritectic crystals (Ol3, Pl3, Cpx3 = MN peritectic crystals; Cpx5 = MD peritectic crystal). For M1 and M2 we distinguish between restitic crystals (Ol2, Pl2, Opx2, and Ox2) and peritectic crystals (Ol3). In this manner, > 95% of the crystals in our run products can be reliably classified. Table 6 offers a summary of experimental reactants and products.

3. Results

3.1. Crystallization experiment

Crystallization of the basaltic–andesitic glass at 1085 °C produces olivine (~5 vol.%), plagioclase (~25 vol.%), clinopyroxene (~5 vol.%), and glass (~65 vol.%) (experiment C1; [Table 2] and [Table 6]; Fig. 3a). All phases are homogeneously distributed throughout the charge. Olivine is subhedral to euhedral and unzoned, with abundant glass inclusions. Crystal sizes are typically ≤ 25 μm. Both plagioclase and clinopyroxene are subhedral to euhedral, unzoned, and ≤ 5 μm in diameter. Plagioclase has length-to-width ratios of ~ 1:2 to 1:3. Olivine is ~ Fo_{83}, plagioclase is ~ An_{60} and contains relatively high K_2O, and clinopyroxene is ~ $En_{54}Fs_7Wo_{39}$ with X_{Mg} values of ~ 89 (Table 4). The glass of the charge is andesitic, calc-alkalic and has a medium- to high-K_2O content (Table 5). Mineral-melt partition coefficients are ~ 0.30 for olivine Fe/Mg, ~ 0.18 for clinopyroxene Fe/Mg, and ~ 1.57 for plagioclase Ca/Na (Table 5). They are in the range of published values, but our Fe/Mg mineral-melt distribution coefficient determined for clinopyroxene is relatively low (e.g., [Sisson and Grove, 1993], [Pichavant et al., 2002] and [Di Carlo et al., 2006]).

3.2. Contamination experiments

3.2.1. Melanorite contamination

Run products of the MN contamination experiment comprise xenocrystic olivine, plagioclase, orthopyroxene, and oxides (~12 vol.%), peritectic olivine, plagioclase, and clinopyroxene (~5 vol.%), primary magmatic olivine, plagioclase, and clinopyroxene (~24 vol.%), and glass (~59 vol.%) (experiment C2; [Table 2] and [Table 6]; Fig. 3b–g). Xenocrysts are ≤ 170 μm and commonly 50–100 μm in size. Peritectic and primary magmatic crystals are typically ≤ 50 μm in size.

Primary magmatic olivine forms single subhedral to euhedral, unzoned or reversely zoned crystals (Fig. 3c,g). Plagioclase is subhedral to euhedral, has length-to-width ratios of ~ 1:2 to 1:3, and sharp core-rim reverse zoning with irregular to round cores (Fig. 3g). Clinopyroxene

is subhedral to euhedral and has sharp core-rim reverse zoning with round cores (Fig. 3c,g). Olivine is $\sim$ Fo$_{90}$, plagioclase has $\sim$ An$_{62}$ core and $\sim$ An$_{74}$ rim composition (Table 4). Clinopyroxene cores have $\sim$ En$_{54}$Fs$_{7}$Wo$_{39}$ composition and X$_{Mg}$ values of $\sim$ 90; rims were too narrow for analysis (Table 4). Relative to crystals of the crystallization experiment, olivine is Fo-rich ($\sim$ Fo$_{90}$ versus Fo$_{83}$) and plagioclase rims are An-rich ($\sim$ An$_{74}$ versus An$_{60}$). Cores of magmatic clinopyroxene in C2 and C1 have identical composition.

Olivine xenocrysts exhibit healed micro-fractures throughout cores and rims with both euhedral crystal faces and irregular embayments (Fig. 3b). They have asymmetric, $\sim$ 30 μm wide high-forsterite rims and $\sim$ 20 μm wide gradational core-rim zones (Fig. 3b). Plagioclase is angular, has minor embayments, and locally sharp, $\leq$ 20 μm wide low-anorthite rims (Fig. 3c). Orthopyroxene is subhedral to round and unzoned (Fig. 3d,f). Both plagioclase and orthopyroxene xenocrysts also contain healed micro-fractures, which terminate at plagioclase core boundaries and at orthopyroxene grain boundaries. Relics of oxide xenocrysts (<1 vol.%) are present within some clusters of peritectic olivine. They are small, anhedral, and have a spongy-cellular texture. Xenocrystic olivine, plagioclase, and orthopyroxene core compositions are equivalent to those the starting material crystals (Table 3). Olivine cores have $\sim$ Fo$_{78}$ composition. Rims have $\sim$ Fo$_{90}$ composition and are thus compositionally indistinguishable from primary magmatic crystals of the charge. Cores of xenocrystic plagioclase have $\sim$ An$_{80}$; their rims have $\sim$ An$_{74}$ composition as rims of primary magmatic plagioclase. Orthopyroxene is $\sim$ En$_{78}$Fs$_{20}$Ws$_{2}$ and has X$_{Mg}$ values of $\sim$ 80. Largely resorbed oxide xenocrysts were too small for quantitative analysis.

Peritectic crystals form clusters of olivine–plagioclase–clinopyroxene (Fig. 3d,f), olivine–plagioclase (Fig. 3e), and olivine ($\pm$ oxides) (Fig. 3f). Olivine of the clusters is subhedral to euhedral and largely unzoned, but rare crystals show weak reverse zoning (e.g., Ol3 marked in Fig. 3d). Melt inclusions are common (Fig. 3e,f,h). Peritectic plagioclase is subhedral to euhedral, unzoned, and randomly oriented (Fig. 3d,e). Length-to-width ratios vary between $\sim$ 1:2 and 1:5. Clinopyroxene is subhedral to euhedral, randomly oriented, and present only in contact with orthopyroxene xenocrysts (Fig. 3d,f). Major- and minor-element compositions of peritectic olivine are identical to C2 primary magmatic crystals and xenocryst rims ($\sim$ Fo$_{90}$). Plagioclase is relatively An-rich (inferred from BSE images), but was too small for analysis. Clinopyroxene core compositions are $\sim$ En$_{45}$Fs$_{7}$Wo$_{49}$ with X$_{Mg}$ values of $\sim$ 87.

The glass of the charge has a basaltic–andesitic, calc-alkalic, and medium-K$_2$O composition. Concentrations of SiO$_2$, TiO$_2$, FeO, and K$_2$O are lower, but concentrations of Al$_2$O$_3$, MgO, CaO, and Na$_2$O are higher than those of the crystallization experiment glass (Table 5). Mineral-melt partition coefficients are $\sim$ 0.32 for olivine Fe/Mg, $\sim$ 0.36 for clinopyroxene Fe/Mg, and $\sim$ 3.51 for plagioclase Ca/Na (Table 5), all higher than those of the C1 run products.

3.2.2. Monzodiorite contamination

Run products of our MD contamination experiment (C3) comprise xenocrystic olivine, plagioclase, and orthopyroxene (~12 vol.%), peritectic olivine, plagioclase, and clinopyroxene (~6 vol.%), primary magmatic olivine, plagioclase, and clinopyroxene (~23 vol.%), and glass (~59 vol.%) ([Table 2] and [Table 6]; Fig. 3h–j). Primary magmatic olivine is present as subhedral crystals in C2, but with larger grain size and higher Fo content than olivine of the previous experiment (Fo$_{94}$ in C3 versus $\sim$ Fo$_{90}$ in C2; Table 4). Plagioclase and clinopyroxene

are texturally and compositionally identical to primary magmatic crystals of MN contamination experiment C2 (Table 4).

Xenocrystic plagioclase derived from the MD has a spongy-cellular texture (Fig. 3h,j). Crystals have relatively An-poor cores (too small to be analyzed) and anorthite-rich rims (~ An_{83}; Table 4). Inherited olivine, orthopyroxene, and plagioclase xenocrysts have euhedral to round crystal shapes and zoning as the equivalent crystals in the MN contamination experiment (Fig. 3h,j). Plagioclase and clinopyroxene have unmodified compositions, but olivine rims have higher Fo content (~ Fo_{94} in C3 versus ~ Fo_{90} in C2). Orthopyroxene xenocrysts are smaller, whereas olivine and plagioclase xenocrysts have sizes indistinguishable from those of C2. Peritectic clinopyroxene derived from the MD contaminant is subhedral to euhedral and forms randomly-oriented monomineralic clusters (Fig. 3i). Crystals are higher in wollastonite (~ Wo_{54}) and X_{Mg} (~ 95) than primary magmatic or MN-derived peritectic clinopyroxene (~ Wo_{49} and X_{Mg} ~ 87; Table 4). Inherited peritectic crystals appear texturally largely unmodified from the previous experiment, but olivine is on average larger and partly encloses neighbouring crystals. Peritectic olivine is Fo-rich (~ Fo_{94}) compared to crystals of the previous experiment (~ Fo_{90}); peritectic plagioclase and clinopyroxene are compositionally unmodified.

The glass of the charge has andesitic, calc-alkalic, and medium-K_2O composition. Compared to glass of the MN contamination experiment, concentrations of CaO, Na_2O, and FeO are lower, while concentrations of SiO_2 and MgO are higher (Table 5). Mineral-melt partition coefficients are ~ 0.38 for olivine Fe/Mg, ~ 0.73 for clinopyroxene Fe/Mg, and ~ 3.20 for plagioclase Ca/Na (Table 5). They are higher than those of both C1 and C2 run products.

3.3. Melting experiments

Melting of the amphibole–phlogopite MN at 1.1 wt.% H_2O (M1) yields 51 vol.% restitic crystals, 16 vol.% peritectic crystals, and 33 vol.% glass (Table 2; Fig. 3k). At 2.1 wt.% H_2O (M2), melting produces 36 vol.% restitic crystals, 14 vol.% peritectic crystals, and 50 vol.% glass (Table 2; Fig. 3). Grain sizes, grain shapes, and zoning patterns of restitic crystals and peritectic crystal are indistinguishable from the equivalent crystal types of our contamination experiments, but peritectic crystals exclusively consist of olivine (Table 2; Fig. 3k,l). Core compositions of restitic olivine, plagioclase, and orthopyroxene are identical to crystals of the starting material. Rims of restitic and peritectic olivine have ~ Fo_{85}, and ~ Fo_{86} in M1 and M2, respectively (Table 4). The glasses have a basaltic to basaltic–andesitic, alkali-calcic, and medium- to high-K_2O composition (Table 5). Olivine-melt Fe/Mg partition coefficients are ~ 0.27 and ~ 0.38 for M1 and M2 (Table 5). The olivine-melt partition coefficient for M1 is lower than those of charges C1 to C3; the partition coefficient for M2 is similar to charge C3.

4. Discussion

4.1. Experimental conditions

Before we proceed to discuss our experimental results, we consider potential limitations of the study due to constant heat supply, short run durations, and Fe loss. We also briefly compare textures, zoning patterns, and compositions of experimental xenocrysts and those of natural TSP lavas. Constant heat supply during our experiments dictates that they are most applicable to natural systems in which the heat required for assimilation reactions is effectively buffered

by the system (i.e., where contaminant mass is small compared to magma mass or where both contaminants and magmas have high initial temperatures; e.g., Spera and Bohrson, 2001).

Short run durations could have prevented our experiments from reaching equilibrium. However, crystals of C1 are subhedral to euhedral, unzoned, compositionally homogeneous and evenly distributed indicating that equilibrium was probably closely approached (cf., Pichavant et al., 2002). Our melting and contamination experiments were designed to mimic disequilibrium textures and short run durations were therefore desired. Nevertheless, we consider the implications of textural and compositional re-equilibrations of xenocryst and peritectic crystals with longer reaction/magma residence times throughout the discussion. We also note that primary magmatic crystals in C2 and C3 are in disequilibrium with their host melt. They show high and increasing Ca/Na_{Pl1-Gl}, $Fe/Mg_{Cpx1-Gl}$ and Fe/Mg_{Ol1-Gl} values (Table 5). High-An of magmatic plagioclase in C2 is interpreted as the incongruent reaction product of crystals inherited from C1 (Table 4). High-An plagioclase crystals in C3 are probably inherited from C2. Primary magmatic clinopyroxene of C2 and C3 is largely inherited from C1, as suggested by their rounded cores, identical composition in all three experiments, and continuously increasing clinopyroxene-melt partition coefficients (Table 5). Olivine–glass partition coefficients show the smallest increase from C1 to C3 (Table 5), which we interpret as due to diffusive re-equilibration between crystals and melt.

Experimental Fe loss decreased FeO and increased X_{Mg} in our run products. The absence of oxides from crystallization experiment C1 may also reflect Fe loss. Mass-balance calculations for C1, M1, and M2 run products give low residuals for ~ 26 to 44% Fe loss (Table 5). From C2 to C3, FeO of olivine decreased by ~ 37% and FeO of glass decreased by ~ 47% ([Table 4] and [Table 5]). Because 5 wt.% MD contamination in C3 may have decreased FeO of the charge by < 3%, we estimate that Fe loss was probably ~ 35–45% in these experiments. Without Fe loss, we estimate that magmatic and peritectic olivine in C2 and C3 would have ~ Fo_{86} (instead of Fo_{90} and Fo_{94}) and that xenocrysts would also show reverse zoning (with ~ Fo_{78} cores). Core composition of natural and experimental olivine xenocrysts is comparable, but the natural xenocrysts show a wider compositional range (~ Fo_{85-75}) than olivine of our contaminants (~ Fo_{78}). Normal zoning of olivine xenocrysts in TSP lavas (Fig. 2b–d; Costa and Dungan, 2005) is likely explained by assimilation (or re-equilibration) at temperatures lower than those of our experiments (i.e., at ~ 1030–1070 °C; Erdmann et al., 2008).

4.2. Textures and assimilation of xenocrysts

Xenocrysts of the original MN and MD assemblages are variably assimilated in our contamination experiments (Table 6; Fig. 4). Largely assimilated xenocrysts are MN-derived oxides and orthopyroxene and MD-derived plagioclase. Oxide xenocrysts are small, round to irregular spongy-cellular-textured, and lack reaction rims. They are present in the first contamination experiment (C2), but absent from the second contamination experiment (C3), which suggests that they were assimilated in > 1 and ≤ 2 days. Orthopyroxene xenocrysts are round, lack reaction rims, and have low X_{Mg} relative to olivine and clinopyroxene of the charges, indicating disequilibrium and partial assimilation (cf. [Obata et al., 1974] and [Brey and Kohler, 1990]). They are present in both contamination experiments, but are unlikely to survive residence times of more than a few days to weeks at the conditions studied. Plagioclase xenocrysts derived from the MD contaminant have a spongy-cellular texture, and anhedral, An-poor cores. With time, An-poor cores of such xenocrysts completely decompose to spongy-cellular, An-rich plagioclase that may subsequently dissolve or anneal to boxy-cellular crystals (e.g., [Johannes et al., 1994] and [Nakamura and Shimakita, 1998]).

Refractory xenocrysts are olivine and plagioclase derived from the MN. They have subhedral to euhedral rims with major- and minor-element compositions identical to those of primary magmatic crystals of the charge (C2: $\sim Fo_{90}$, $\sim An_{74}$; C3: $\sim Fo_{94}$, $\sim An_{73}$), indicating that they are in local equilibrium with their host melt. Evidence for significant dissolution prior to rim formation is lacking. Olivine xenocrysts develop reverse zoning with $\sim Fo_{78}$ cores and $\sim Fo_{90}$ or $\sim Fo_{94}$ rims (in C2 and C3; Table 4; Fig. 3b,e,h). Plagioclase xenocrysts develop normal zoning with $\sim An_{80}$ cores and $\sim An_{74}$ rims (Table 4; Fig. 3c). Xenocrysts that develop such texturally and compositionally distinct rims, or reaction rims, have been previously described in both experiments and nature (e.g., [Tsuchiyama, 1986], [Rutherford and Hill, 1993], [Murphy et al., 2000], [Coombs and Gardner, 2004], [Beard et al., 2005], [Erdmann et al., 2007] and [Streck, 2008]). They may form by primary magmatic crystallization, incongruent melting or dissolution, diffusive re-equilibration, or a combination of these processes. Gradational core-rim zoning of olivine xenocrysts in our C2 and C3 experiments indicates that diffusive re-equilibration took place (Fig. 3b,e,h). The relatively variable width of Fo-rich olivine rims may point to formation in an incongruent reaction between olivine and iddingsite, such as Ol1/Id1 $\rightarrow$ Ol2 $\pm$ L (L = liquid, Id = iddingsite; Fig. 3b). The relatively constant width of plagioclase rims may be the result of either primary magmatic crystallization or an incongruent reaction.

4.3. Formation, textures, and composition of peritectic crystals

In our experiments peritectic crystals provide evidence for both MN and MD contaminants (Table 6; Fig. 4). Those of the MN contamination experiment may have formed through decomposition of amphibole, biotite, or iddingsite, and in reaction with orthopyroxene or oxides (Fig. 4b,c). Amphibole and iddingsite are the only assimilated components that contain appreciable amounts of CaO. Amphibole accounts for most of the assimilated xenocrysts (~27 vol.% of MN contaminant), whereas iddingsite is volumetrically minor (<10 vol.% of Ol1 and $\leq$ 1.5 vol.% MN contaminant) (Table 2). We therefore suggest that amphibole xenocrysts decomposed to olivine and plagioclase peritectic crystal clusters in a reaction of the type Amph2 + L1 $\rightarrow$ $\sim$ 0.3 Ol3 + $\sim$ 0.3 Pl3 + $\sim$ 0.4 L2 (L = liquid). Weak reverse core-rim zoning of the large peritectic olivine crystals (e.g., Ol3 marked in Fig. 3d) may reflect Fe loss during the experiment or progressive orthopyroxene or oxide dissolution. For the second most common cluster type, consisting of olivine $\pm$ oxides, phlogopite xenocrysts are the likely precursors, assimilated in a melting reaction of the form Bt2 $\pm$ Ox2 $\pm$ L1 $\rightarrow$ $\sim$ 0.6 Ol3 + $\sim$ 0.4 L2 $\pm$ Ox2. Iddingsite probably decomposed in a comparable melting reaction of the type Id2 $\pm$ Ox2 $\pm$ L1 $\rightarrow$ $\sim$ 0.6 Ol3 $\pm$ $\sim$ 0.4 L2, and mostly contributed to the growth of Fo-rich rims on olivine xenocrysts (see Section 4.2). Relic oxide xenocrysts are interpreted as partly-decomposed oxide inclusions. Finally, clusters consisting of olivine, plagioclase, and clinopyroxene occur only in contact with orthopyroxene (Fig. 3d,f). We suggest that these clusters formed by decomposition of amphibole in contact with orthopyroxene, where orthopyroxene contributed Si to stabilize clinopyroxene.

Peritectic crystal clusters formed in C2 survive in C3, where olivine crystals are on average larger than in C2. This may indicate growth by textural annealing, primary magmatic overgrowths on peritectic crystal cores, or both. Peritectic crystals of the MD contamination experiment are clinopyroxene (Cpx5) cluster (Fig. 4e). Peritectic clinopyroxene may have formed through assimilation of MD-derived clinopyroxene or biotite partly replaced by chlorite, or oxides, or in a reaction with inherited components. We suggest that clinopyroxene partly replaced by chlorite provided a fertile and H_2O-bearing reactant to form peritectic

clinopyroxene in a reaction of the type Cpx4 + Chl4 ± L1 → ~ 0.7 Cpx5 + ~ 0.4 L2 (L = liquid). Biotite and oxides were completely assimilated.

In our experiments, peritectic crystals thus replaced hydrous or altered xenocrysts. Anhydrous xenocrysts decomposed congruently (Opx2, Ox2, Ox4, Pl4, Qtz4, and Kfs4) or developed incongruent or primary magmatic overgrowths (Ol2, Pl2; Figs. 3b,c, 4c,e). These observations are in agreement with findings from natural igneous rocks (e.g., [Stewart, 1975], [Couch et al., 2001], [Amma-Miyasaka and Nakagawa, 2002] and [Beard et al., 2005]). They imply that only contaminants with hydrous assemblages may form abundant peritectic crystals, while contaminants dominated by anhydrous assemblages will largely contribute xenocrysts or partial melt to a magma.

4.4. Progressive assimilation of xenocrysts and peritectic crystals

Xenocrysts in volcanic rocks that had short magma residence times of hours to a few days may texturally resemble the xenocrysts of our experiments, showing anhedral grain shapes owing to resorption or subhedral to euhedral grain shapes reflecting growth. Reactive xenocrysts with magma residence times of days to weeks are likely to be completely assimilated. Refractory xenocrysts that form reaction rims or overgrowths probably survive assimilation. With long magma residence times or significant growth, originally sharp core-rim zoning will become diffuse in most xenocryst types and for most elements. In such cases, zoning patterns of slow-diffusing elements and mineral textures (i.e., deformation features, inclusion types and patterns) may be the best guides for identifying xenocrystic cores.

Peritectic crystals in volcanic rocks that had short magma residence times of hours to a few days may resemble the experimentally-produced peritectic crystals in grain shape, grain size, and lack of zoning (Fig. 5a,e). Peritectic crystals with longer magma residence times likely anneal into larger crystals and develop primary magmatic overgrowths (Fig. 5b–h). Single-mineral clusters may coarsen to subhedral or euhedral crystals (Fig. 5a–d), possibly with complex patchy zoning and exotic inclusions (Fig. 5d). Clusters made up of more than one crystal type may coarsen to aggregates with few individual crystals (Fig. 5e–h). Texturally, such crystals and crystal clusters may be indistinct from primary magmatic phenocrysts. For fast-diffusing elements in olivine (or other rapidly equilibrating minerals), compositional zoning will be affected by diffusive re-equilibration. For clinopyroxene or slow-diffusing species in olivine, patchy to skeletal zoning may reveal cores made up of peritectic crystals. Because the contaminant starting materials of our experiments were dominated by xenocrysts rather than micro-xenoliths, peritectic crystals derived from single minerals are most abundant. In nature, country-rock xenoliths (including micro-xenoliths) are volumetrically more important than xenocrysts, at least during early stages of assimilation, and peritectic crystals derived from two or more minerals may thus be most common.

Core-rim and patchy zoning may be important textural characteristics of xenocrysts and peritectic crystals, but they are not unique to crystals derived from country-rock contamination. Melt or other inclusions, mineral trace-element and isotopic compositions are likely essential to distinguish xenocrysts and peritectic crystals formed through country-rock contamination from cognate, primary magmatic crystals and those derived from magma mixing or replacement of primary magmatic crystals, antecrysts, or source-inherited solids (e.g., [Stewart, 1975], [Couch et al., 2001], [Amma-Miyasaka and Nakagawa, 2002], [Beard et al., 2004], [Beard et al., 2005] and [Streck, 2008]).

4.5. Role of host magmas

Different peritectic crystal assemblages in MN melting and MN contamination experiments indicate that the host melt affected their crystallization. Melanorite contamination of the BA, on one hand, produces peritectic olivine, olivine–plagioclase, and olivine–plagioclase–clinopyroxene. The peritectic crystals are immersed in a relatively SiO_2-rich melt, from which plagioclase and clinopyroxene crystallize ([Table 1] and [Table 5]). Melanorite melting, on the other hand, produces olivine as the only peritectic mineral and SiO_2-poor, initially H_2O-saturated melt ([Table 1] and [Table 5]). Plagioclase and clinopyroxene do not form. This suggests that host melt and decomposing xenocrysts diffusively equilibrate. One specific contaminant type may therefore form variable peritectic crystal assemblages in different host magmas. The larger the compositional contrast between host melt and contaminants, the more significant is the effect.

5. Conclusions

Experiments of the type described here are a powerful tool to aid in the identification of components of open-system magma evolution. In our contamination experiments, anhydrous xenocrysts either develop overgrowths in equilibrium with their host magma and thereby survive assimilation, or they decompose. Hydrous xenocrysts and xenocrysts altered by hydrous phases (e.g., by chlorite or iddingsite) decompose to peritectic crystals and melt. We suggest that in naturally-contaminated igneous rocks, peritectic crystals should also be abundant, provided contamination involves rocks with hydrous assemblages. Peritectic crystals with short magma residence times likely have compositions and textures that are distinct from the primary magmatic crystals of their host, forming clusters of one or more mineral types. Peritectic crystals with long magma residence times may have grain shapes and zoning patterns identical to those of primary magmatic crystals (i.e. euhedral shapes, core-rim zoning in major elements), but may show patchy zoning patterns for slow-diffusing elements and possibly exotic melt or other inclusions.

Acknowledgements

References

Amma-Miyasaka and Nakagawa, 2002 M. Amma-Miyasaka and M. Nakagawa, Origin of anorthite and olivine megacrysts in island-arc tholeiites: petrological study of 1940 and 1962 ejecta from Miyake–Jima volcano, Izu–Mariana arc, *Journal of Volcanology and Geothermal Research* **117** (2002), pp. 263–283.

Beard et al., 2005 J.S. Beard, P.C. Ragland and M.L. Crawford, Reactive bulk assimilation: a model for crust–mantle mixing in silicic magmas, *Geology* **33** (2005), pp. 681–684

Beard et al., 2004 J.S. Beard, P.C. Ragland and T. Rushmer, Hydration crystallization reactions between anhydrous minerals and hydrous melt to yield amphibole and biotite in igneous rocks: description and implications, *Journal of Geology* **112** (2004), pp. 617–621.

Behrens and Gaillard, 2006 H. Behrens and F. Gaillard, Geochemical aspects of melts; volatiles and redox behavior, *Elements* **2** (2006), pp. 275–280.

Brey and Kohler, 1990 G.P. Brey and T. Kohler, Geobarometry in four-phase lherzolites II. New thermobarometers, and practical assessment of existing thermobarometers, *Journal of Petrology* **31** (1990), pp. 1353–1378.

Clarke, 2007 D.B. Clarke, Assimilation of xenocrysts in granitic magmas; principles, processes, proxies, and problems, *Canadian Mineralogist* **45** (2007), pp. 5–30.

Coombs and Gardner, 2004 M. Coombs and J. Gardner, Reaction rim growth on olivine in silicic melt: Implications for magma mixing, *American Mineralogist* **89** (2004), pp. 748–759.

Costa and Dungan, 2005 F. Costa and M. Dungan, Short time scales of magmatic assimilation from diffusion modeling of multiple elements in olivine, *Geology* **33** (2005), pp. 837–840.

Costa et al., 2002 F. Costa, M. Dungan and B. Singer, Hornblende- and phlogopite-bearing gabbroic xenoliths from Volcan San Pedro (36°S), Chilean Andes: evidence for melt and fluid migration and reactions in subduction-related plutons, *Journal of Petrology* **43** (2002), pp. 219–241

Costa et al., 2004 F. Costa, B. Scaillet and M. Pichavant, Petrologic and phase equilibria constraints on the pre-eruption conditions of Holocene dacite from Volcan San Pedro (36°S, Chilean Andes) and the importance of sulfur in silicic subduction-related magmas, *Journal of Petrology* **45** (2004), pp. 855–881.

Couch et al., 2001 S. Couch, R.S.J. Sparks and M.R. Carroll, Mineral disequilibrium in lavas explained by convective self-mixing in open magma chambers, *Nature* **411** (2001), pp. 1037–1039.

Di Carlo et al., 2006 I. Di Carlo, M. Pichavant, S. Rotolo and B. Scaillet, Experimental crystallization of high-K arc basalts: the golden pumice, Stromboli volcano (Italy), *Journal of Petrology* **47** (2006), pp. 1317–1343.

Davidson et al., 2007 J. Davidson, S. Turner, H. Handley, C. Macpherson and A. Dosseto, Amphibole "sponge" in arc crust?, *Geology* **35** (2007), pp. 787–790.

Dungan and Davidson, 2004 M. Dungan and J. Davidson, Partial assimilative recycling of the mafic plutonic roots of arc volcanoes: an example from the Chilean Andes, *Geology* **32** (2004), pp. 773–776.

Dungan et al., 2001 M.A. Dungan, A. Wulff and R. Thompson, Eruptive stratigraphy of the Tatara–San Pedro complex, 36°S, Southern volcanic zone, Chilean Andes: reconstruction method and implications for magma evolution at longlived arc volcanic centers, *Journal of Petrology* **42** (2001), pp. 555–626.

Erdmann et al., 2009 S. Erdmann, R.A. Jamieson and M.A. MacDonald, Evaluating the origin of garnet, cordierite, and biotite in granitic rocks: a case study from the South Mountain Batholith, Nova Scotia, *Journal of Petrology* **50** (2009), pp. 1477–1503.

Erdmann et al., 2007 S. Erdmann, D. London, G.B. Morgan VI and D.B. Clarke, Contamination of granitic magma by metasedimentary country-rock material: an experimental study, *Canadian Mineralogist* **45** (2007), pp. 43–61

Erdmann et al., 2008 S. Erdmann, B. Scaillet and M. Dungan, Temperature–composition conditions of country-rock assimilation in basalts from the Tatara–San Pedro volcanic complex, *GAC-MAC Annual Meeting, Abstracts with Programs* (2008), p. 53.

Gaillard et al., 2002 F. Gaillard, B. Scaillet and M. Pichavant, Kinetics of iron–oxidation–reduction in hydrous silicic melts, *American Mineralogist* **87** (2002), pp. 829–837

Gonzàlez and Vergara, 1962 O. Gonzàlez and M. Vergara, Reconocimiento geológico de la Cordillera de los Andes entre los paralelos 35° y 38° latitud sur, *Universidad de Chile, Instituto de Geología, Publicaciones 24* (1962), p. 121.

Hall et al., 2004 L.J. Hall, J. Brodie, B.J. Wood and M.R. Carroll, Iron and water losses from hydrous basalts contained in $Au_{80}Pd_{20}$ capsules at high pressure and temperature, *Mineralogical Magazine* **68** (2004), pp. 75–81

Iacono-Marziano et al., 2007 G. Iacono-Marziano, F. Gaillard and M. Pichavant, Limestone assimilation and the origin of CO_2 emissions at the Alban Hills (Central Italy): constraints from experimental petrology, *Journal of Volcanology and Geothermal Research* **165** (2007), pp. 91–105.

Johannes et al., 1994 W. Johannes, J. Koepke and H. Behrens, Partial melting reactions of plagioclases and plagioclase-bearing systems. In: I. Parsons, Editor, *Feldspars and Their Reactions*, Kluwer Academic Publishers, Dordrecht (1994), pp. 161–194.

Kawamoto and Hirose, 1994 T. Kawamoto and K. Hirose, Au–Pd sample containers for melting experiments on iron and water bearing systems, *European Journal of Mineralogy* **6** (1994), pp. 381–385.

Kretz, 1983 R. Kretz, Symbols for rock-forming minerals, *American Mineralogist* **68** (1983), pp. 277–279.

Lackey et al., 2006 J.S. Lackey, S. Erdmann, D.B. Clarke, K.L. Fellah, R.M. Nowak, M. Spicuzza and J.W. Valley, Oxygen isotope evidence for the origin of garnet in the peraluminous South Mountain Batholith, Nova Scotia, *Geological Society of America Annual Meeting, Abstracts with Programs* **38** (2006), p. 113.

Murphy et al., 2000 M.D. Murphy, R.S.J. Sparks, J. Barclay, M.R. Carroll and T.S. Brewer, Remobilization of andesite magma by intrusion of mafic magma at the Soufriere Hills Volcano, Montserrat, West Indies, *Journal of Petrology* **41** (2000), pp. 21–42.

Nakamura and Shimakita, 1998 M. Nakamura and S. Shimakita, Dissolution origin and syn-entrapment compositional change of melt inclusion in plagioclase, *Earth and Planetary Science Letters* **161** (1998), pp. 119–133.

Nelson et al., 1999 S.T. Nelson, J.P. Davidson, M.T. Heizler and B.J. Kowallis, Tertiary tectonic history of the southern Andes: the subvolcanic sequence to the Tatara–San Pedro volcanic complex, lat 36°S, *Geological Society of America Bulletin* **111** (1999), pp. 1387–1404.

Obata et al., 1974 M. Obata, S. Banno and T. Mori, The iron–magnesium partitioning between naturally occurring coexisting olivine and Ca-rich clinopyroxene: an application of the simple mixture model to olivine solid solution, *Bulletin de la Société Française de Minéralogie et de Cristallographie* **97** (1974), pp. 101–107.

Pownceby and O'Neill, 1994 M.I. Pownceby and H.St.C. O'Neill, Thermodynamic data from redox reactions at high temperatures. III. Activity–composition relations in Ni–Pd alloys from EMF measurements at 850–1250 K, and calibration of the NiO + Ni–Pd assemblage as a redox sensor, *Contributions to Mineralogy and Petrology* **116** (1994), pp. 327–339.

Pichavant et al., 2002 M. Pichavant, C. Martel, J.-L. Bourdier and B. Scaillet, Physical conditions, structure and dynamics of a zoned magma chamber: Mt. Pelée (Martinique, Lesser Antilles Arc), *Journal of Geophysical Research* **107** (2002), p. 2093.

Rutherford and Hill, 1993 M.J. Rutherford and P.M. Hill, Magma ascent rates from amphibole breakdown: an experimental study applied to the 1980–1986 Mount St. Helens eruptions, *Journal of Geophysical Research* **80** (1993), pp. 19667–19685.

Scaillet and Evans, 1999 B. Scaillet and B. Evans, The 15 June 1991 eruption of Mount Pinatubo. I. Phase equilibria and pre-eruption P–T–fH_2O–fO_2 conditions of the dacite magma, *Journal of Petrology* **40** (1999), pp. 381–411

Scaillet et al., 1995 B. Scaillet, M. Pichavant and J. Roux, Experimental crystallization of leucogranite magmas, *Journal of Petrology* **36** (1995), pp. 663–705.

Singer et al., 1995 B.S. Singer, M.A. Dungan and S.D. Layne, Textures and Sr, Ba, Mg, Fe, K, and Ti compositional profiles in volcanic plagioclase: clues to the dynamics of calc-alkaline magma chambers, *American Mineralogist* **80** (1995), pp. 776–798.

Singer et al., 1997 B.S. Singer, R.A. Thompson, M.A. Dungan, T.C. Feeley, S.T. Nelson, J.C. Pickens, L.L. Brown, A.W. Wulff, J.P. Davidson and J. Metzger, Volcanism and erosion during the past 930 k.y. at the Tatara–San Pedro complex, Chilean Andes, *Geological Society of America Bulletin* **109** (1997), pp. 127–142.

Sisson and Grove, 1993 T.W. Sisson and T.L. Grove, Experimental investigation of the role of H_2O in calc-alkaline differentiation and subduction zone magmatism, *Contributions to Mineralogy and Petrology* **113** (1993), pp. 143–166.

Spear, 1993 F.S. Spear, Metamorphic Phase-Equilibria and Pressure–Temperature–Time Paths, Mineralogical Society of America Publication, Washington, D. C. (1993).

Spera and Bohrson, 2001 F.J. Spera and W.A. Bohrson, Energy-constrained open-system magmatic processes; I, general model and energy-constrained assimilation and fractional crystallization (EC-AFC) formulation, *Journal of Petrology* **42** (2001), pp. 999–1018

Stephens, 2001 W.E. Stephens, Polycrystalline amphibole aggregates (clots) in granites as potential I-type restite: an ion microprobe study of rare-earth distributions, *Australian Journal of Earth Sciences* **48** (2001), pp. 591–601

Stevens et al., 2007 G. Stevens, A. Villaros and J.-F. Moyen, Selective peritectic garnet entrainment as the origin of geochemical diversity in S-type granites, *Geology* **35** (2007), pp. 9–12

Stewart, 1975 D.C. Stewart, Crystal clots in calc-alkaline andesites as breakdown products of high-Al amphiboles, *Contributions to Mineralogy and Petrology* **53** (1975), pp. 195–204.

Streck, 2008 M.J. Streck, Mineral textures and zoning as evidence for open system processes, *Reviews in Mineralogy and Geochemistry* **69** (2008), pp. 595–622.

Tsuchiyama, 1986 A. Tsuchiyama, Experimental study of olivine-melt reaction and its petrological implications, *Journal of Volcanology and Geothermal Research* **29** (1986), pp. 245–264.
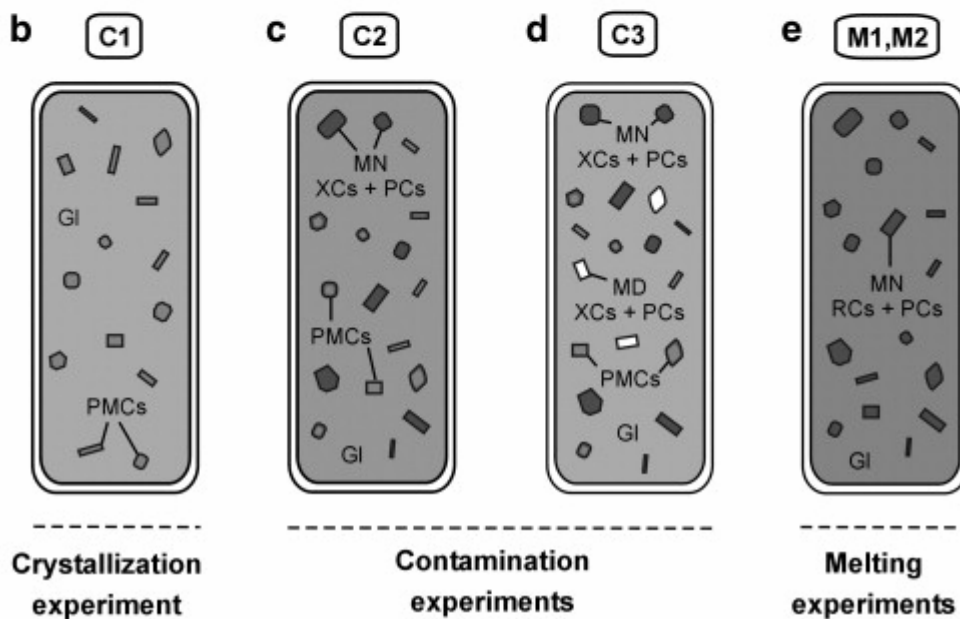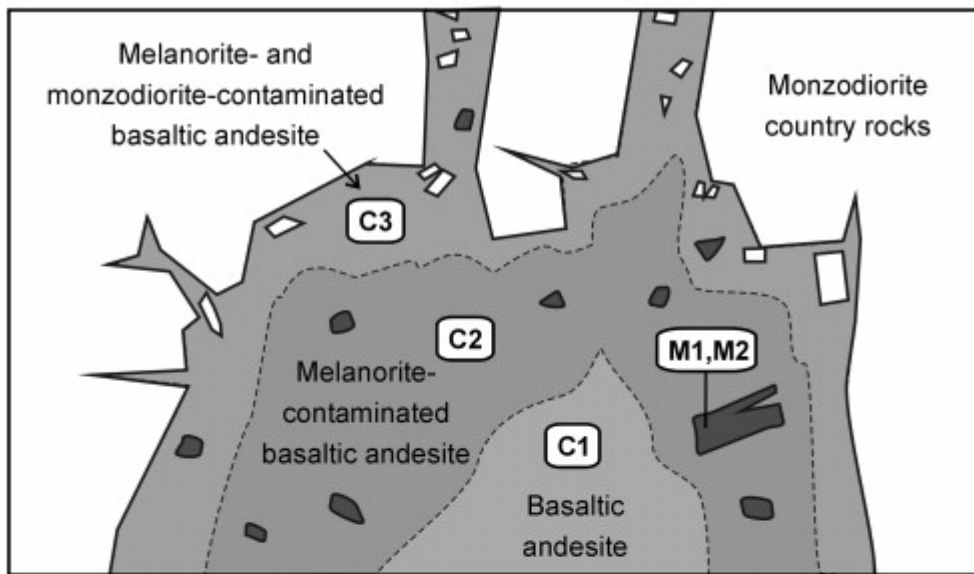
Figures

Fig. 1. Sketch illustrating country-rock contamination and melting mimicked in our experiments (C1, C3, C3, M1, and M2). Details of experimental starting materials and run products are summarized in [Table 1], [Table 2] and [Table 6]. (a) Possible natural scenario, where melanorite contamination preceded monzodiorite contamination. (b–e) Crystallization, contamination, and melting experiments. Gl = glass; MN = melanorite; MD = monzodiorite; PMCs = primary magmatic crystals; XCs = xenocrysts; PCs = peritectic crystals; and RCs = restitic crystals.
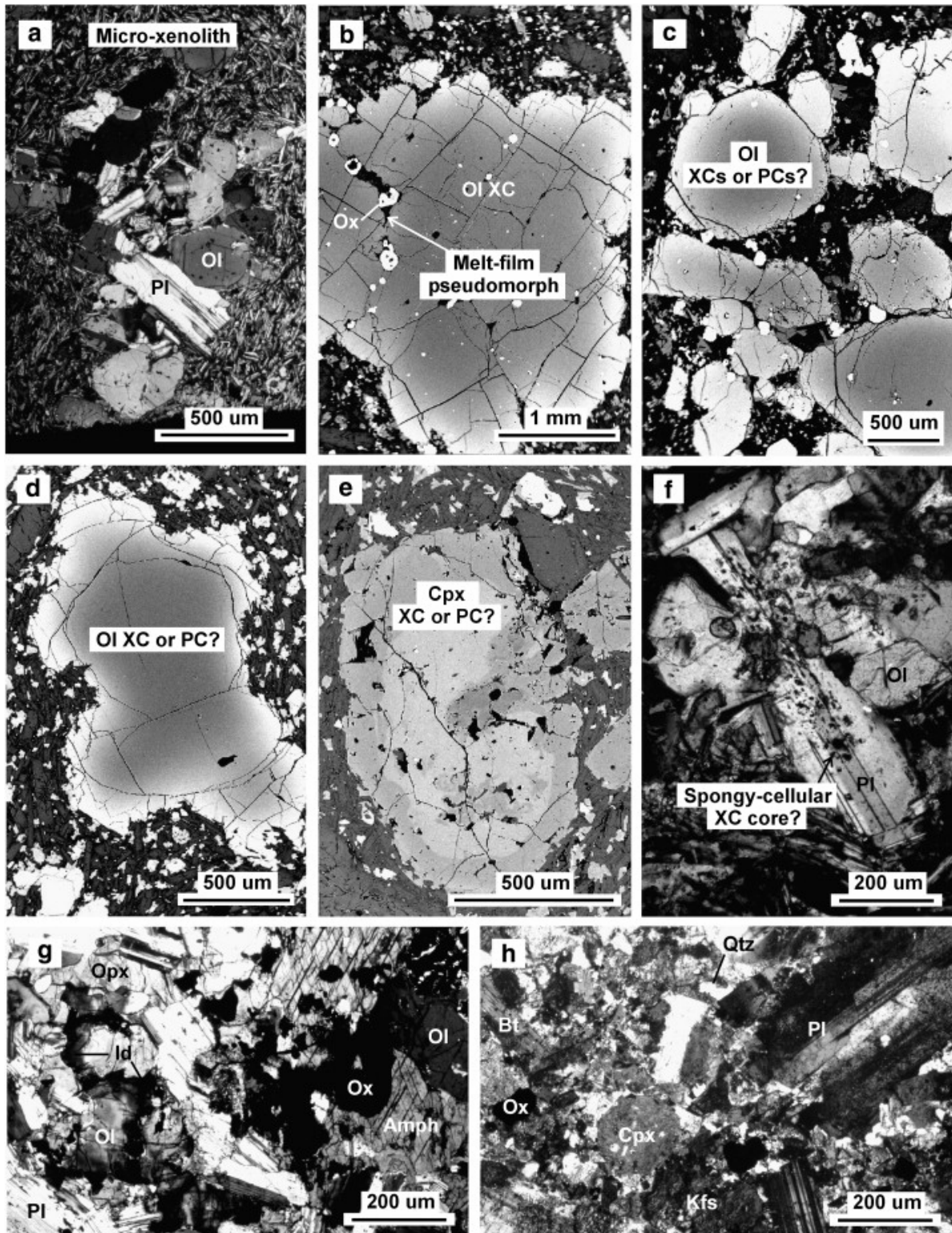
Fig. 2. Micro-photographs (a,f–h) and back-scattered electron (BSE) images (b-e) of micro-xenoliths, xenocrysts, and potential peritectic crystals in TSP lavas. (a) Olivine–plagioclase micro-xenolith with subsolidus deformation features (e.g., deformation twins in Pl). (b) Olivine xenocryst with irregular grain boundaries and melt-film pseudomorph. (c,d) Potential olivine xenocryst(s) or peritectic crystal(s). Note that olivine normal zoning contrasts with reverse zoning of experimental olivine xenocrysts. This likely indicates assimilation at lower temperature, or re-equilibration in TSP lavas (Erdmann et al., 2008). (e) Subhedral, complexly zoned clinopyroxene xenocryst or peritectic crystal. (f) Cluster of olivine and plagioclase with spongy-cellular-textured cores. (g) Melanorite and (h) monzodiorite starting rocks (TSP dacite xenoliths). Ox = oxide; Id = iddingsite. All other mineral abbreviations follow those of (Kretz, 1983) and (Spear, 1993).

PMCs - Ol1, Pl1, Cpx1   MN XCs/RCs - Ol2, Pl2, Opx2, Ox2   MN PCs - Ol3, Pl3, Cpx3   MD XC - Pl4   MD PC - Cpx5
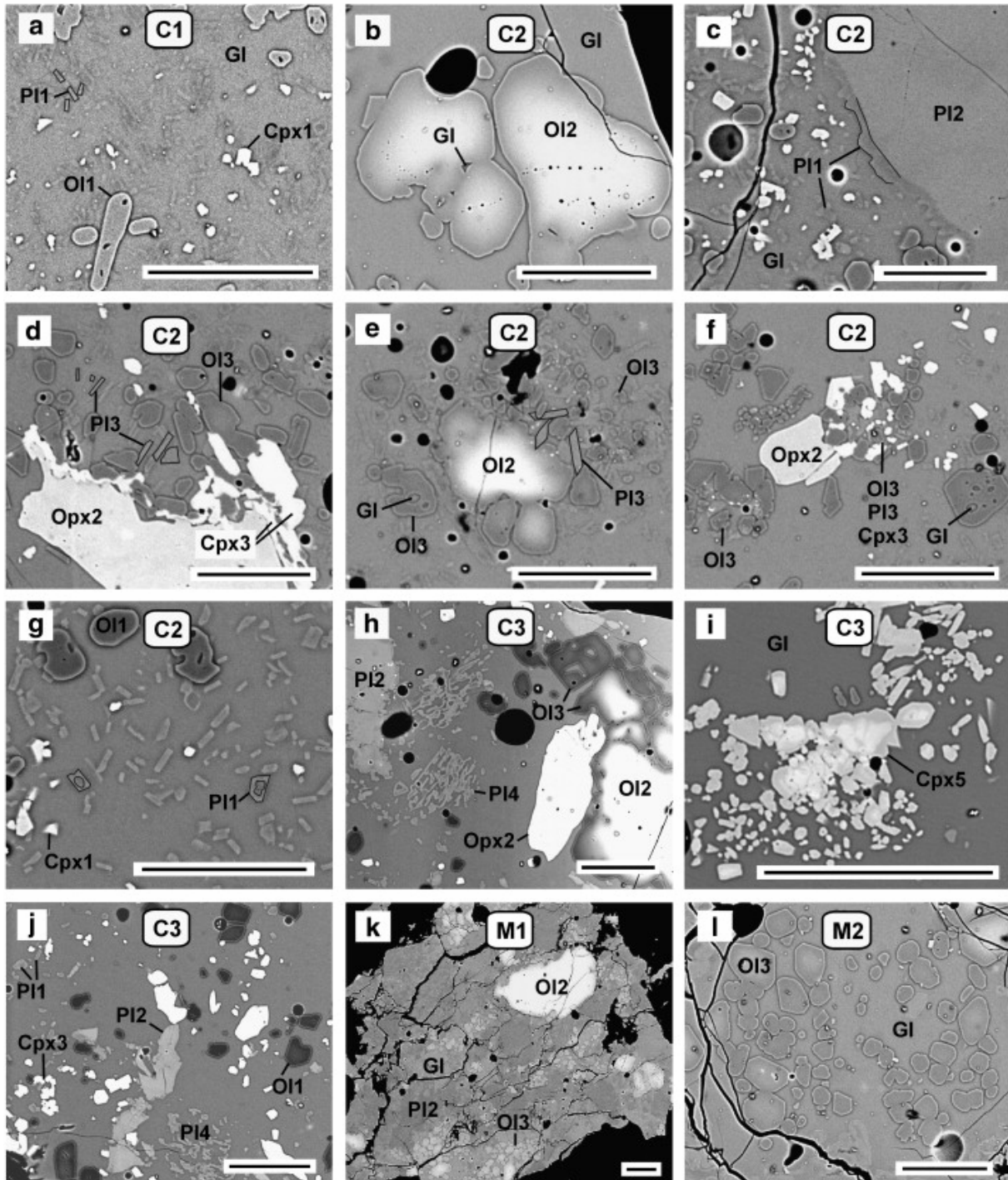
Fig. 3. BSE images of experimental run products. (a) Contamination experiment C1: crystallization of the basaltic–andesitic starting glass. (b–g) Contamination experiment C2: contamination of the BA by 25 wt.% MN. (h–j) Contamination experiment C3: contamination of C2 by 5 wt.% MD. (k,l) Experiments M1 and M2: Melanorite partial melting with (k) ~ 1.1 wt.% and (l) ~ 2.1 wt.% H_2O added. All scale bars are 50 μm. PMCs = primary magmatic crystals; XCs = xenocrysts; PCs = peritectic crystals. Solid lines in a–c–d–e partly outline plagioclase.
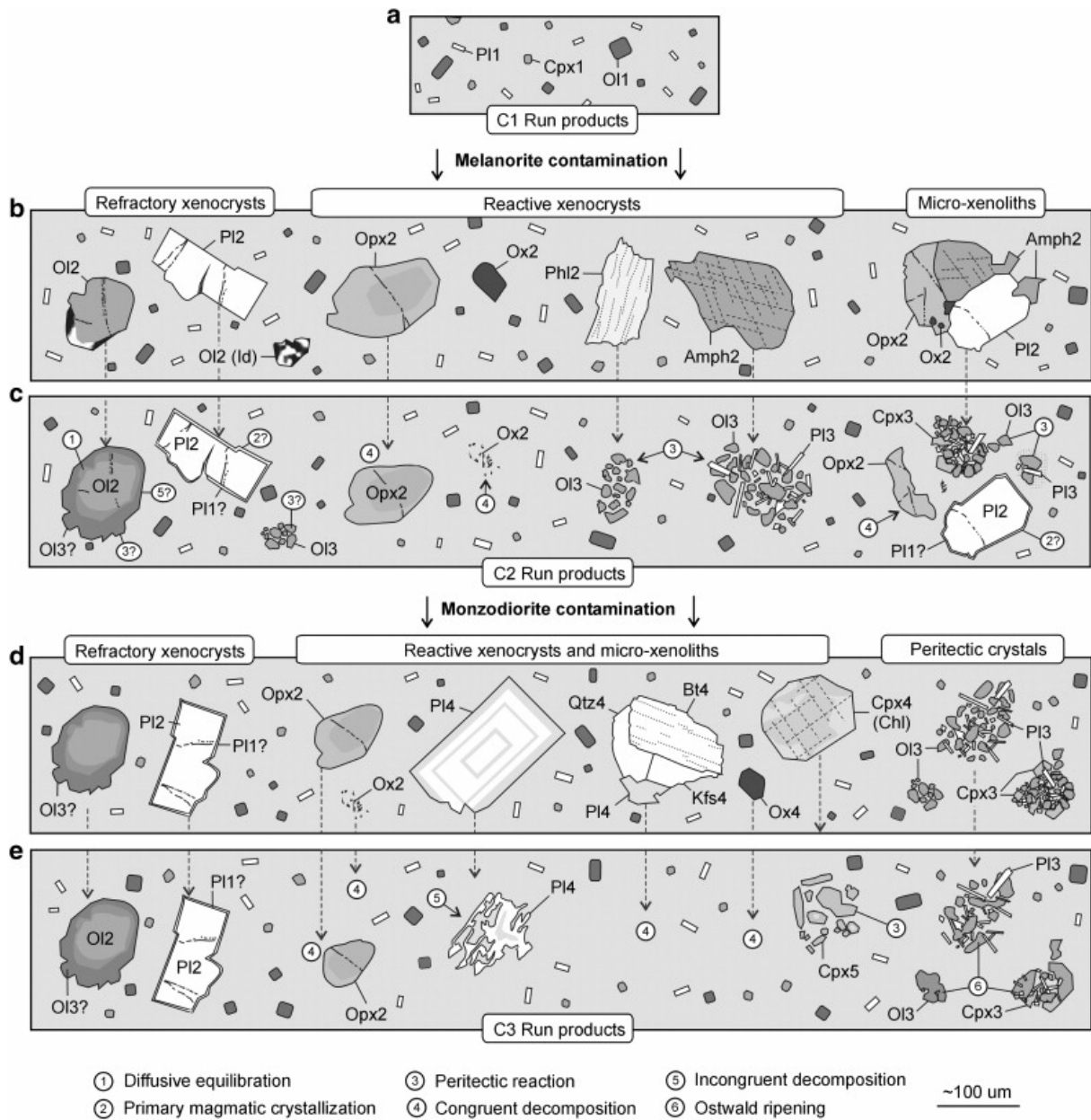
Fig. 4. Sketch illustrating starting materials and run products of experiments C1 to C3, and our interpretation of assimilation processes during the experiments. (a) C1 run products of the partially crystallized BA; (b) C2 starting material employing the crystallized BA and 25 wt.% of the melanorite contaminant; (c) C2 run products; (d) C3 starting material employing the C2 run product and 5 wt.% of the MD contaminant; and (e) C3 run products. Dashed arrows highlight evolution of individual contaminants in C2 (b → c) and C3 (d → e). Mineral classification is summarized in Table 6.
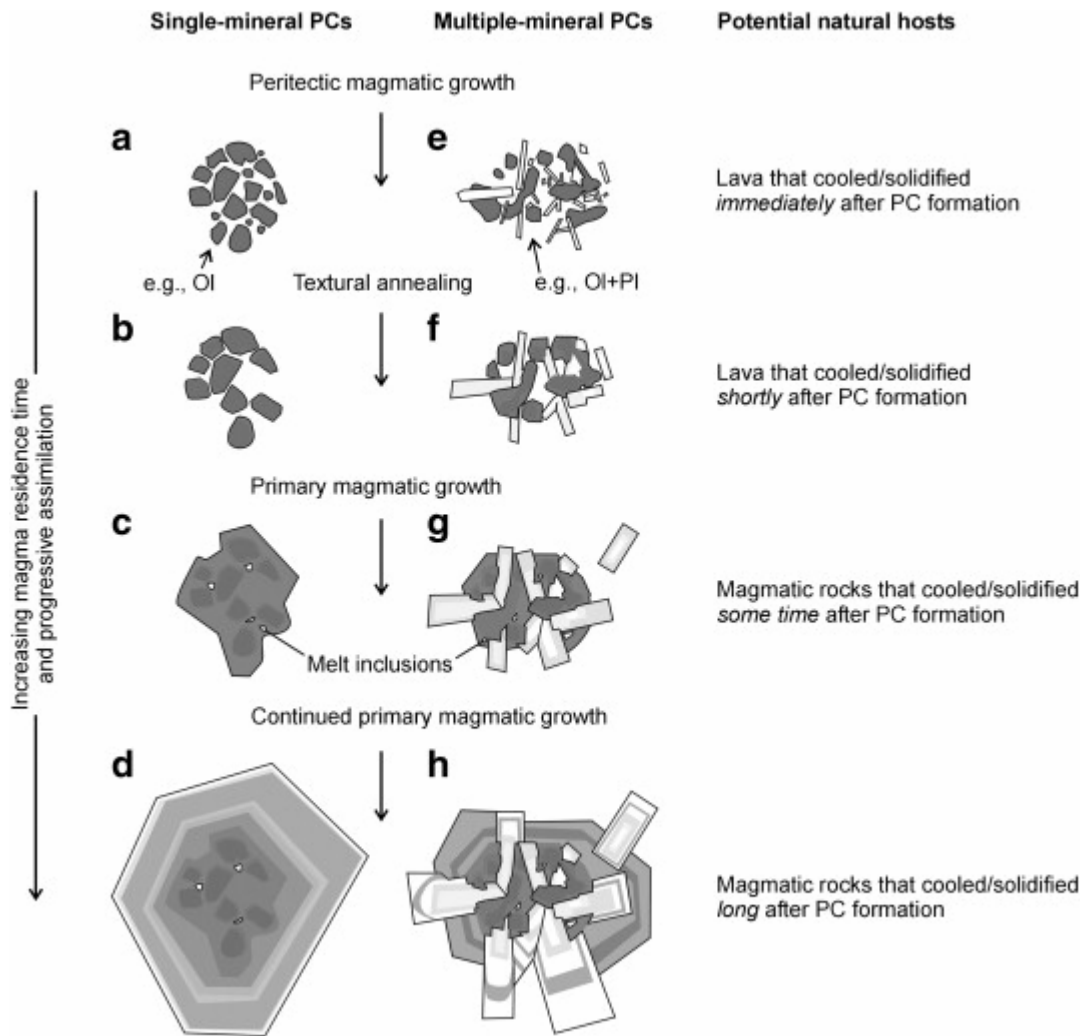
Fig. 5. Proposed progressive assimilation of peritectic crystals (PCs) with increasing magma residence time. Different grey shades of minerals symbolize different mineral compositions. (a,b) Initial formation of peritectic crystal clusters as those produced in C2. (b,f) Peritectic crystal clusters texturally anneal. (c–h) With increasing magma residence time, textures and chemical features of natural peritectic crystals likely progressively mimic those of primary magmatic crystals. Patchy zoning may be the best guide to reveal peritectic crystals. Melt or other inclusions may be necessary evidence to distinguish peritectic crystals formed through contamination from those formed by magma mixing, from source-inherited restite, or early differentiates.

Table 1. Starting material compositions.

Material	BA	MN	MD	Mix C2	Mix C3
wt.%					
SiO_2	55.04	45.69	62.73	52.70	53.20
TiO_2	0.81	0.44	0.55	0.72	0.71
Al_2O_3	17.54	22.29	18.62	18.73	18.72
Fe_2O_3[a]	8.28	7.76	3.86	8.15	7.94
MnO	0.12	0.11	0.08	0.12	0.12
MgO	6.06	10.73	1.44	7.23	6.94
CaO	7.48	10.56	3.71	8.25	8.02
Na_2O	3.63	2.11	4.96	3.25	3.34
K_2O	1.17	0.46	3.45	0.99	1.12
P_2O_5	0.23	0.07	0.16	0.19	0.19
Total	100.36	100.22	99.55	100.32	100.29
ppm					
V	144.2	105.9	46.3	134.6	130.2
Cr	144.3	331.0	10.3	191.0	181.9
Co	32.4	63.6	5.9	40.2	38.5
Ni	76.2	223.5	9.6	113.0	107.9
Cu	53.5	33.9	44.1	48.6	48.4
Zn	60.6	68.1	48.8	62.5	61.8
Ga	17.8	13.9	19.4	16.8	17.0
Rb	37.1	18.3	126.0	32.4	37.1
Sr	505.8	635.4	404.5	538.2	531.5
Y	17.5	6.6	25.0	14.8	15.3
Zr	121.2	33.9	511.3	99.4	120.0
Nb	5.2	0.7	4.1	4.1	4.1
Ba	316.3	162.9	777.8	278.0	302.9

Material	BA	MN	MD	Mix C2	Mix C3
La	18.9	6.2	31.4	15.7	16.5
Pb	7.3	0.4	18.8	5.6	6.2
Th	0.0	0.0	13.6	0.0	0.7
U	2.0	1.4	2.2	1.9	1.9
Ce	37.3	10.3	56.4	30.6	31.8
Nd	18.6	4.4	24.2	15.1	15.5
Cs	0.0	0.0	7.6	0.0	0.4

Analyses of BA (basaltic andesite), MN (melanorite), and MD (monzodiorite) starting materials were carried out at the Saint Mary's University Regional Geochemical Centre, using a Phillip's PW2400 X-ray spectrometer. Mix C2 = 75 wt.% BA + 25 wt.% MN; Mix C3 = 95 wt.% Mix C2 + 5 wt.% MD. Mix compositions calculated from BA, MN, and MD analyses.

[a] All Fe reported as Fe_2O_3.

Table 2. Mineralogy of starting materials and experimental run products (vol.%).

Starting materials
BA: Gl(100)
MN: Pl(45),Amph(27),Ol(15)[a],Opx(5),Phl(5),Ox(3)
MD: Pl(55),Kfs(24),Qtz(8),Bt(5)[b],Cpx(5)[b],Ox(2),Ep(< 1)
Run products melting experiments
M1: Gl(33),Ol2(10),Ol3(16),Pl2(38),Opx2(2),Ox2(1)
M2: Gl(50),Ol2(9),Ol3(14),Pl2(27),Ox2(< 1)
Run products crystallization experiment
C1: Gl(65),Pl1(25),Ol1(5),Cpx1(5)
Run products contamination experiments
C2: Gl(59),Pl1(17),Pl2(8),Pl3(1),Ol1(3),Ol2(3),Ol3(4),Cpx1(4),Cpx3(< 1),Opx2(1),Ox2(< 1)
C3: Gl(59),Pl1(16),Pl2(8),Pl3(1),Pl4(1),Ol1(3),Ol2(3),Ol3(4),Cpx1(4),Cpx3(1),Cpx5(< 1),Opx2(< 1)

Mineralogy estimated from thin sections and BSE images. BA = basaltic andesite; MN = melanorite; MD = monzodiorite; Gl = glass; M1 = MN + 1.1 wt.% H_2O; M2 = MN + 2.1 wt.% H_2O; C1 = BA glass + 1.5 wt.% H_2O; C2 = C1 + 25 wt.% MN; and C3 = C2 + 5 wt.% MD. Mineral abbreviations follow those of (Kretz, 1983) and (Spear, 1993). [a] partly replaced by iddingsite; [b] partly replaced by chlorite. [Fig. 2] and [Fig. 3] show microphotographs of starting materials and run products. Table 6 provides a list of all crystal types and their main characteristics.

Table 3. Representative contaminant mineral compositions.

Material	MN		MN		MN		MN		MN	
Mineral	Pl		Amph		Ol		Opx		Phl	
(wt.%)	n = 6	σ	n = 5	σ	n = 4	σ	n = 3	σ	n = 7	σ
SiO_2	47.35	0.96	42.91	0.52	38.64	0.09	54.60	0.26	38.40	0.45
TiO_2	–	–	2.78	0.42	0.02	0.02	0.18	0.00	2.11	0.53
Al_2O_3	32.93	0.52	11.46	0.44	0.01	0.01	0.94	0.11	15.89	0.40
FeO[a]	0.21	0.03	8.44	0.13	19.59	0.34	12.68	0.70	8.65	0.66
MnO	0.01	0.01	0.16	0.06	0.38	0.04	0.41	0.01	0.07	0.03
MgO	0.03	0.01	15.60	0.31	40.09	0.12	28.38	0.13	20.01	0.43
CaO	16.23	0.63	10.87	0.18	0.01	0.01	0.96	0.01	0.02	0.01
Na_2O	2.18	0.36	2.53	0.07	0.00	0.00	0.04	0.00	1.56	0.21
K_2O	0.04	0.02	0.52	0.05	0.02	0.02	0.02	0.02	7.64	0.36
BaO	0.00	0.01	–	–	–	–	–	–	0.24	0.08
NiO	–	–	0.03	0.03	0.12	0.01	0.05	0.01	0.10	0.03
Cr_2O_3	–	–	0.07	0.03	0.02	0.02	0.04	0.04	0.11	0.05
Total	98.96		95.36		98.89		98.29		94.8	
	An = 80	3	X_{Mg} = 77	1	Fo = 78	< 1	En = 78	1	X_{Mg} = 80	1
							Fs = 20	1		
							Wo = 2	< 1		
							X_{Mg} = 80	1		
Material	MD		MD		MD		MD		MD	
Mineral	Pl[b]		Pl[b]		Kfs		Bt[c]		Cpx[c]	
(wt.%)	n = 4	σ	n = 4	σ	n = 4	σ	n = 5	σ	n = 4	σ
SiO_2	54.14	0.06	60.75	0.22	65.75	0.15	36.17	0.04	51.9	0.4
TiO_2	–	–	–	–	–	–	5.71	0.03	–	–
Al_2O_3	28.45	0.27	24.52	0.22	18.43	0.03	13.07	0.05	3.1	0.3

Material	MN		MN		MN		MN		MN	
Mineral	Pl		Amph		Ol		Opx		Phl	
(wt.%)	n = 6	σ	n = 5	σ	n = 4	σ	n = 3	σ	n = 7	σ
FeO[a]	0.55	0.03	0.15	0.05	0.08	0.05	15.73	0.04	17.3	0.4
MnO	0.01	0.01	0.01	0.00	0.01	0.00	0.18	0.01	0.3	0.0
MgO	0.10	0.03	0.00	0.00	0.00	0.00	12.23	0.06	11.6	0.3
CaO	11.43	0.10	6.19	0.29	0.00	0.00	0.00	0.00	12.3	0.1
Na$_2$O	4.90	0.00	7.75	0.30	0.76	0.01	0.38	0.00	0.3	0.0
K$_2$O	0.29	0.02	0.55	0.11	15.51	0.17	8.66	0.02	0.1	0.0
Total	99.86		99.92		100.54		92.12		97.03	
	An = 55	3	An = 30	2	Or = 93	< 1	X$_{Mg}$ = 58	1	En = 38	1
									Fs = 33	1
									Wo = 29	< 1
									X$_{Mg}$ = 54	1

Analyses were performed with a JEOL 8200 electron microprobe at Dalhousie University, operating at 15 keV and 15 nA, with a 2–3 μm spot size, and 40 s counting times. Data are average concentrations (of n analyses) and standard deviation (σ). Fo = (Mg/(Mg + Fe) × 100); An = (Ca/(Ca + Na + K) × 100);
Or = (K/(Ca + Na + K) × 100); En = (Mg/(Mg + Fe + Mn + Ca) × 100);
Fs = ((Fe + Mn)/(Mg + Fe + Mn + Ca) × 100); Wo = Ca/(Mg + Fe + Mn + Ca) × 100).
X$_{Mg}$ = (Mg/(Mg + Fe) × 100).

[a] All Fe reported as FeO.
[b] Representative range of plagioclase compositions.
[c] Low total reflects partial alteration.

Table 4. Composition of experimental olivine, plagioclase, and clinopyroxene.

Mineral	Ol1[a]		Ol1[a]		Ol1[a]		Ol3[a]		Ol3[a]		Pl1		Pl1[b]	
Run	C1		C2		C3		M1		M2		C1		C2	
(wt. %)	n = 4	σ	n = 5	σ	n = 10	σ	n = 4	σ	n = 5	σ	n = 4	σ	n = 3	σ
SiO_2	39.92	0.23	40.91	0.52	40.85	0.33	37.14	0.55	39.25	0.15	55.17	0.19	53.71	0.65
TiO_2	0.04	0.02	0.01	0.01	0.01	0.02	0.02	0.01	0.00	0.00	–	–	–	–
Al_2O_3	0.13	0.20	0.07	0.10	0.10	0.19	0.00	0.00	0.02	0.02	27.42	0.11	27.31	0.82
FeO[c]	15.49	0.41	9.26	0.61	5.80	0.64	14.14	0.92	12.99	0.70	0.41	0.01	0.37	0.24
MnO	0.29	0.02	0.25	0.02	0.24	0.03	0.27	0.02	0.18	0.02	0.03	0.01	0.01	0.01
MgO	43.84	0.21	49.26	0.26	52.07	0.91	45.16	0.95	45.87	0.64	0.57	0.10	0.85	0.04
CaO	0.35	0.13	0.18	0.05	0.23	0.10	0.27	0.01	0.19	0.04	12.02	0.20	12.27	0.65
Na_2O	0.03	0.02	0.02	0.01	0.02	0.02	0.01	0.00	0.00	0.00	4.10	0.04	3.88	0.13
K_2O	0.03	0.01	0.02	0.00	0.02	0.01	0.02	0.00	0.02	0.00	0.41	0.01	0.42	0.05
NiO	0.04	0.02	0.03	0.02	0.04	0.03	–	–	–	–	–	–	–	–
Cr_2O_3	0.04	0.03	0.01	0.01	0.02	0.04	0.03	0.01	0.00	0.00	–	–	–	–
Total	100.19		100.02		99.39		97.07		98.52		100.12		98.81	
	Fo = 83	< 1	Fo = 90	1	Fo = 94	1	Fo = 85	1	Fo = 86	1	An = 60	1	An = 62	2

Mineral	Pl1[d]	Pl1[d]	Pl4[e]	Cpx1[a]	Cpx1[a]	Cpx 3[a]	Cpx 1[a]		Cpx 1[a]

Mineral	Ol1[a]		Ol1[a]		Ol1[a]		Ol3[a]		Ol3[a]		Pl1			Pl1[b]
Run	C1		C2		C3		M1		M2		C1			C2
(wt. %)	n = 4	σ	n = 5	σ	n = 10	σ	n = 4	σ	n = 5	σ	n = 4		σ	n = 3
Run	C2		C3		C3		C1		C2		C2	C3		C3
(wt. %)	n = 3	σ	n = 4	σ	n = 3	σ	n = 4	σ	n = 4	σ	n = 2	n = 7	σ	n = 3
SiO_2	50.38	3.49	50.60	2.35	46.82	0.68	53.99	1.01	54.06	0.47	52.96	52.90	0.77	53.86
TiO_2	–	–	–	–	–	–	0.72	0.07	0.61	0.08	0.26	0.54	0.17	0.59
Al_2O_3	30.28	2.17	30.59	0.96	32.56	0.58	4.26	0.95	2.92	0.11	1.21	2.30	0.68	2.87
FeO_a	0.28	0.11	0.09	0.01	0.12	0.02	3.72	0.15	3.90	1.31	4.24	3.96	0.90	1.61
MnO	0.01	0.01	0.00	0.00	0.00	0.00	0.20	0.00	0.24	0.05	0.14	0.25	0.03	0.19
MgO	0.52	0.28	0.36	0.16	0.24	0.00	17.53	0.79	18.49	0.22	15.77	18.55	0.45	18.82
CaO	14.93	1.98	14.74	0.86	16.55	0.74	17.57	0.88	18.30	0.70	23.94	19.08	1.00	21.12
Na_2O	2.73	1.01	2.89	0.58	1.78	0.38	0.45	0.14	0.30	0.02	0.15	0.26	0.04	0.30
K_2O	0.25	0.12	0.20	0.07	0.12	0.01	0.06	0.02	0.07	0.01	0.02	0.03	0.01	0.04
NiO	0.01	0.00	–	–	–	–	0.02	0.00	0.03	0.02	0.03	0.02	0.04	0.00
Cr_2O_3	–	–	–	–	–	–	0.87	0.05	0.68	0.19	0.06	0.55	0.21	1.33
Total	99.38		99.46		98.18		99.40		99.61		98.77	98.44		100.73
	An = 74	6	An = 73	5	An = 83	3	En = 54	< 1	En = 54	< 1	En = 45	En = 53	< 1	En = 43
							Fs =	<	Fs =	2	Fs =	Fs =	2	Fs =

Mineral	Ol1[a]		Ol1[a]		Ol1[a]		Ol3[a]		Ol3[a]		Pl1		Pl1[b]	
Run	C1		C2		C3		M1		M2		C1		C2	
(wt. %)	n = 4	σ	n = 5	σ	n = 10	σ	n = 4	σ	n = 5	σ	n = 4	σ	n = 3	σ
							7	1	7		7	7		3
							Wo = 39	< 1	Wo = 39	2	Wo = 49	Wo = 40	2	Wo = 54
							X_{Mg} = 89	1	X_{Mg} = 90	3	X_{Mg} = 87	X_{Mg} = 89	2	X_{Mg} = 95
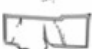
n = number of analyses; σ = standard deviation. [a] Mineral compositions reflect partial Fe loss from experiments; see Table 5 for details. [b] Composition of inherited cores. [c] All Fe reported as FeO. [d] Composition of rims. [e] Compositionally modified, skeletal xenocryst. Table 3 reports analytical conditions; Table 6 summarizes crystal types.

Table 5. Glass compositions of contamination and melting experiments.

Run	C1		C2		C3		M1		M2	
(wt.%)	n = 6	σ	n = 13	σ	n = 20	σ	n = 7	σ	n = 6	σ
SiO_2	57.39	0.72	56.85	1.17	58.40	0.56	51.22	0.26	49.21	0.31
TiO_2	1.35	0.09	1.09	0.08	1.09	0.08	1.21	0.03	0.83	0.03
Al_2O_3	17.37	0.12	18.59	1.19	18.25	0.63	19.20	0.15	20.74	0.15
FeO^a	4.55	0.29	2.43	0.20	1.28	0.09	5.71	0.25	4.59	0.54
MnO	0.14	0.02	0.11	0.04	0.09	0.04	0.13	0.01	0.12	0.01
MgO	3.86	0.16	4.12	0.28	4.40	0.19	4.85	0.33	6.16	0.11
CaO	6.47	0.25	7.02	0.41	6.81	0.33	8.08	0.12	8.87	0.16
Na_2O^b	3.46	0.44	4.51	0.17	4.27	0.05	4.18	0.11	4.25	0.14
K_2O	2.05	0.21	1.67	0.11	1.73	0.10	1.61	0.04	1.16	0.04
P_2O_5	0.30	0.04	0.26	0.03	0.23	0.02	–	–	–	–
F	0.08	0.08	0.08	0.09	0.12	0.12	–	–	–	–
Total	97.02		96.73		96.66		96.19		95.93	
X_{Mg}	60	< 1	75	< 1	86	1	60	2	71	3
X_{Ca}	43	1	42	2	41	2	46	< 1	49	< 1
Fe/Mg_{Ol1-Gl}	0.30		0.32		0.38		0.27		0.38	
$Fe/Mg_{Cpx1-Gl}$	0.18		0.36		0.73		–		–	
Ca/Na_{Pl1-Gl}	1.57		3.51		3.20		–		–	
ΔFeO (%)^c	− 44 [0.36]		− 35 to 45		− 35 to 45		− 26 [0.27]		− 36 [0.95]	

Analyses were performed with a JEOL 733 electron microprobe at the Ontario Museum of Nature, operating at 15 keV and 10 nA, with a 10 μm spot size, and 25 s counting times on background and peaks. Data are average concentrations (of n analyses) and standard deviation (σ). [a] All Fe reported as FeO. [b] Corrected relative to glass standards of Scaillet and Evans (1999). Mineral–glass Fe/Mg distribution coefficients are calculated for total Fe as FeO. [c] Apparent Fe loss calculated as $100 \times (FeO_{Charge} − FeO_{St.Mat.})/FeO_{St.Mat.}$. FeO_{Charge} calculated from crystals and glass. St.Mat.= starting material. Residuals (ΣR^2) obtained in mass-balance calculations given in parentheses. Fe loss for C2 and C3 is estimated from glass FeO and olivine FeO compositions.

Table 6. Summary of experimental reactants and products and their main characteristics.

Reactant	Product	Main characteristics	St. Mat.
Amph2	Ol3-Pl3±Cpx3+L	Large, angular, unzoned single crystals	MN
Ol2	Ol2+Ol3±L	Large, angular, unzoned zoned single crystals; iddingsite rims	MN
Opx2	Opx2+L	Large, angular, largely unzoned single crystals	MN
Ox2	Ox2+L	Small, anhedral, unzoned single crystals and inclusions	MN
Phl2	Ol3+L	Large, angular to subhedral, unzoned single crystals	MN
Pl2	Pl2±L	Large, angular, unzoned single crystals	MN
Bt4	L	Large, angular to subhedral, unzoned single crystals	MD
Cpx4	Cpx5+L	Large, anhedral, unzoned single crystals; partly chloritized	MD
Kfs4	L	Small, angular, unzoned single crystals	MD
Ox4	L	Small, anhedral, unzoned single crystals	MD
Pl4	Pl4+L	Small to large, angular, normally zoned single crystals	MD
Qtz4	L	Small, angular, unzoned single crystals	MD

Product	Crystal type	Main characteristics	Experiment
Cpx1	PM	Small, euhedral, unzoned to reversely zoned single crystals	C1-C3
Ol1	PM	Small, sub- to euhedral, unzoned to reversely zoned single crystals	C1-C3
Pl1	PM	Small, sub- to euhedral, unzoned to reversely zoned single crystals	C1-C3
Ol2	XC/RC	Large, subhedral, reversely zoned single crystals	C2,C3,M1,M2
Opx2	XC/RC	Large to small, anhedral, largely unzoned single crystals	C2,C3,M1,M2
Ox2	XC/RC	Small, spongy-cellular, unzoned single crystals	C2,M1,M2
Pl2	XC/RC	Large, angular to subhedral, normally zoned single crystals	C2,C3,M1,M2
Pl4	XC	Small, spongy-cellular, reversely zoned single crystals	C3
Cpx3[a]	PC	Small, sub-to euhedral, unzoned crystals; cluster	C2,C3
Ol3	PC	Small, sub- to euhedral, unzoned crystals; cluster	C2,C3,M1,M2
Pl3[b]	PC	Small, sub- to euhedral, unzoned crystals; cluster	C2,C3
Cpx5	PC	Small, sub- to euhedral, reversely zoned crystals; cluster	C3

Mineral abbreviations follow those of Kretz (1993) and Spear (1993). L = Liquid. Relative grain size variations of crystal types approximately to scale. [a] Cpx3 shown with Ol3 adn Pl3; [b] Pl3 shown with Ol3. MN = melanorite; MD = monzodiorite; St. Mat. = starting material; PM = primary magmatic; PC = peritiectic crystal; RC = restitic crystal; and XC = xenocryst.